RSC Advances

ROYAL SOCIETY OF CHEMISTRY

www.rsc.org/advances

[1] Fabrication and photoelectrochemical characteristics of $CuInS_2$ and PbS quantum dots co-sensitized TiO_2 nanorods photoelectrodes

Minmin Han[a,b], Junhong Jia[a,*], Limin Yu[a,b], Gewen Yi[a]

[a] State Key Laboratory of Solid Lubrication, Lanzhou Institute of Chemical Physics, Chinese Academy of Sciences, Lanzhou, 730000, P. R. China.
[b] University of Chinese Academy of Sciences, Beijing, 100080, P. R. China.

* Corresponding author. Tel./Fax: +86-931-4968611.
E-mail address: jhjia@licp.cas.cn (J. Jia)

Abstract

A cascade structured $PbS/CuInS_2/TiO_2$ photoelectrode with the co-sensitizer of $CuInS_2$ and PbS quantum dots (QDs) deposited on TiO_2 nanorods is fabricated *via* successive ionic layer absorption and reaction (SILAR) method. The effects of SILAR cycle numbers of *n* and *m* for $CuInS_2$ QDs and PbS QDs, as well as the influence of co-sensitization of QDs on the energy conversion efficiency, are discussed. The results show that the deposition of co-sensitizer PbS QDs on $CuInS_2$ QDs-TiO_2 nanorod arrays photoelectrode presents a complementary effect in the light absorption. The performance of quantum dots sensitized solar cells (QDSSCs) shows dominant dependence on the value of SILAR cycles *n* and *m*. The enhanced performance of QDSSCs with the cascade structure, $PbS/CuInS_2/TiO_2$ photoelectrode, is attributed to the Fermi energy level alignment of QDs co-sensitizer. An energy conversion efficiency of 4.11% is achieved using the $PbS/CuInS_2/TiO_2$ photoelectrodes under one sun illumination (AM 1.5, 100 $mW \cdot cm^{-2}$).

1. Introduction

In recent decades, there is an urgent demand to explore and develop environmental friendly alternative energy because of the decline of fossil fuels and increasing pollution.[1-4] Solar cells, as a kind of clean energy, are paid more attention in research and application areas. Dye-sensitized solar cells(DSSCs) develop rapidly over the past two decades. They combine both the advantages of organic dye photosensitizers and inorganic semiconductor, and have achieved power conversion efficiency up to 13%.[5] There are inorganic semiconductor quantum dots (QDs)

besides those organic dyes, which can also serve as sensitizers based on quantum confinement effect. On the basis of quantum size effect, optical band edge can be tuned by controlling QDs size, accompanied with the enlarged photoabsorption from visible to near-infrared (n-IR) region.[6] Furthermore, the high extinction coefficient could speed photoinduced charge separation and reduce dark current.[7] In addition, the impact ionization effect enables quantum yield to be more than 100% through generating multiple excitons from single-photon absorption.[8] Therefore, quantum dots sensitized solar cells (QDSSCs) are considered novel candidates for the third generation solar cells.

At present, owing to the suitable/compatible band gap and facile preparation, TiO_2 with a band gap of 3.26 eV is one of the most commonly used photoanode materials for QDSSCs.[9] The recombination of photogenerated electron-hole pair in QDSSCs is restrained because TiO_2 cannot produce holes to combine the electrons due to large band gap. However, its wide band gap also limits the absorption range only to the UV region. Hence, different kinds of semiconductor QDs with narrow band gaps such as CdS,[10-12] CdSe,[13-15] InP,[16] InAs,[17] PbS,[18] Bi_2S_3,[19] and $CuInS_2$,[20-22] are induced to extend the activity of the photoelectrode into the visible light region. As a Ⅰ-Ⅲ-$Ⅵ_2$ inorganic semiconductor compound, $CuInS_2$ has great potential in solar cells due to high absorption coefficient (~10^5 cm^{-1}), optimal band gap (~1.5 eV), good photostability and low cost.[23, 24] Several efforts have been made to develop the synthesis methods, photoelectrochemical characteristics and applications of $CuInS_2$ in solar cells. According to the study of Ren *et al.*, the $CuInS_2$ QDs with size ranging

from 1.8 nm to 5.2 nm were prepared *via* a conventional convective heating method, which could be employed in the low-cost non-vacuum-based solar cells.[29] Kamat *et al.* assembled $CuInS_2$ QDSSCs with an energy conversion efficiency (η) of 1.14% via electrophoretic deposition and further increased the energy conversion efficiency to 3.91% by using CdS as a passivation layer.[25] Teng *et al.* investigated the effect of QD sizes and counter electrodes on the performance of $CuInS_2$-QDs/CdS heterostructure.[26-28] They synthesized the $CuInS_2$ QDs by a hydrothermal process and fabricated the QDs on TiO_2 nanocrystalline followed by coating CdS. The as-prepared QDSSCs exhibited the enhanced photoelectrochemical performance due to the dual role of pillar and passivation layer of CdS.

Although many efforts have been taken to improve the performance of QDSSCs, the η is still extremely lower than that of DSSCs, which is mainly due to the junction between QDs and electron-conducting substrates and the defect density on the QD surface, as well as the difficulty of assembling semiconductor QDs into matrix. As an alternative, utilizing different kinds of QDs as sensitizers (i.e. co-sensitization) has been studied in the past few years. Lee *et al.* enhanced the η of QDSSCs to 4.22% by depositing the co-sensitizer of CdS/CdSe on the mesoscopic TiO_2 films, which is advantageous to the electron injection and hole-recovery of QDs.[35] Zhao *et al.* prepared the core/shell structured $CuInS_2$/CdS on the TiO_2 films and investigated the electron transfer from QDs to TiO_2 by time-resolved photoluminescence spectroscopy. The performance of QDSSCs was improved with the improved electron transfer by passivating surface states and tuning the band alignment of QDs.[20] Recently, Shen and

Katayama *et al.* studied the photoexcited carrier dynamics of co-sensitizer of double-layered CdS/CdSe QDs with heterodyne transient grating and transient absorption methods and they found that the η can be enhanced by 70% in the appropriate layer order and the reverse electron transfer does not matter for the energy conversion efficiency.[36] Therefore, the co-sensitization is a promising approach to improve the performance of QDSSCs, and the key issues are to develop the suitable semiconductor QDs with suitable band gap and panchromatic light absorption range.

PbS, with a bulk band gap in the IR (~0.37 eV), is a particularly interesting semiconductor material. Compared with $CuInS_2$, PbS has low electron injection efficiency due to its lower location of conduction band edge than that of TiO_2,[30] while the conduction band edge of $CuInS_2$ is higher than that of TiO_2.[21] However, PbS can extend the absorption range to ca. 900 nm which is larger than that of $CuInS_2$(ca. 600 nm).[31,32] To take both advantages of the two materials in light harvest and electron injection, $CuInS_2$ and PbS can be used as co-sensitizers of TiO_2 film.

Herein, we prepare $CuInS_2$ QDs and PbS QDs *via* successive ionic layer absorption and reaction (SILAR) method sequentially to sensitize TiO_2 nanorod arrays, and assemble a co-sensitized cascade structure. Influence of SILAR cycle numbers of *n* and *m* for $CuInS_2$ QDs and PbS QDs, microstructure and phase composition, and the co-sensitization of QDs on the energy conversion efficiency of PbS/$CuInS_2$/TiO_2 photoelectrodes are investigated by XRD, FESEM, XPS, TEM-SAED, UV-vis-NIR measurements and Electrochemical workstation equipped with solar simulator. The cascade structure has proved to possess excellent photoelectrochemical characteristics

compared with single $CuInS_2$ or PbS due to the synergistic effect and an energy conversion efficiency of 4.11% is achieved in this work.

2. Experimental Section

2.1. Materials

Analytical-grade concentrated hydrochloric acid (HCl, 36.5%-38% by weight), cupric chloride hemipentahydrate ($CuCl_2 \cdot 2H_2O$, 99%), sodium sulfide ($Na_2S \cdot 9H_2O$, 98%), lead nitrate ($Pb(NO_3)_2$, 99%), zinc acetate ($Zn(CH_3COO)_2 \cdot 2H_2O$, 99%), potassium chloride (KCl, 99.5%), sulfur powder (S, 99.5%), chloroplatinic acid ($H_2PtCl_6 \cdot 6H_2O$, 98%) and high purity indium chloride ($InCl_3$, 99.99%) were purchased commercially and used as received. Titanium chloride ($TiCl_4$, 99%) was purchased from Aldrich. All chemicals were used without further purification.

2.2. Synthesis of TiO_2 Nanorod Arrays

TiO_2 nanorod arrays were prepared on fluorine-doped tin oxide (FTO) glass using a hydrothermal method similar to the literature.[33] Prior to the fabrication of TiO_2 nanorod arrays, the FTO substrate was ultrasonically cleaned for 60 min in a mixed solution of deionized water, acetone and 2-propanol with volume ratios of 1:1:1, subsequently rinsed with deionized water, and finally dried in a nitrogen stream. 15 mL of deionized water was mixed with 15 mL concentrated hydrochloric acid. The mixture was stirred at ambient conditions for 5 min before 0.3 mL of titanium chloride was added and then placed in a Teflon-lined stainless steel autoclave (50 mL volume) after being stirred for another 5 min. After that, one piece of FTO substrate was placed at an angle against the wall of the Teflon liner with the conductive side

facing down. A reaction temperature of 180 ^{o}C was used, with reaction time lasting 2.5 h in oven. After synthesis, the autoclave was water-cooled to room temperature, and then the FTO substrate was taken out, rinsed extensively with deionized water and allowed to dry in ambient air.

2.3. Fabrication of PbS/$CuInS_2$/TiO_2 electrodes

$CuInS_2$ QDs were deposited on TiO_2 nanorods with a modified successive ionic layer absorption and reaction (SILAR) method reported by Cho *et al.*[22]. The deposition was carried out at room temperature. TiO_2 film was dipped into 5 mM $CuCl_2$ aqueous solution for 10 s followed by deionized water washing, and dipped into 50 mM Na_2S aqueous solution for 10 s followed by deionized water washing. Then the TiO_2 film was dipped into 5 mM $InCl_3$ aqueous solution for 10 s followed by deionized water washing, and 50 mM Na_2S aqueous solution for 10 s followed by deionized water washing again. The four-step dipping procedure was termed as one SILAR cycle. The deposited samples were annealed at 500 ^{o}C in nitrogen atmosphere after several SILAR cycles which is different from the subsequent treatment process of Cho *et al.*. The TiO_2 nanorod sample after *n* cycles of $CuInS_2$ deposition was denoted as $CuInS_2$(*n*)/TiO_2. For PbS QDs, the SILAR was used to deposit on the $CuInS_2$(*n*)/TiO_2 photoelectrodes as well. Briefly, the $CuInS_2$(*n*)/TiO_2 photoelectrode was immersed into 0.02 M $Pb(NO_3)_2$ aqueous solution for 30 s followed by deionized water washing, and then immersed for another 30 s into 0.05 M Na_2S aqueous solution and washed again with deionized water. The two-step immersion program was termed as one SILAR cycle. After *m* cycles of PbS deposition, the sensitized

photoelectrode was denoted as PbS(m)/CuInS$_2$(n)/TiO$_2$.

2.4. Fabrication of QDSSCs

The solar cells were assembled into a sandwich-type configuration by placing a Pt-coated counter electrode prepared by spin coating method on the QDs-sensitized TiO$_2$ photoanode with a 60 μm-thick Surlyn sealing material as a spacer. The redox electrolyte used in this study was a polysulfide solution consisting of 0.2 M KCl, 0.5 M Na$_2$S and 2.0 M sulfur in a mixture of methanol and water solution (3:7 by volume).[34] The mixture combines the dissolving capacity of solvent and penetration to the working electrode. The addition of KCl improves the conductive capability of solvent.[27] The active area of the solar cells was 0.5 cm^2.

2.5. Measurements

The surface morphologies of the as-prepared samples were examined using a field emission scanning electron microscopy (FESEM, JSM-6701F, Japan). Transmission electron microscopy (TEM) and high-resolution transmission electron microscopy (HRTEM, FEI Tecnai F30, acceleration voltage: 300 kV) were used to explore the microstructure of the QDs. The structure and phase composition were analyzed by powder X-ray diffraction (XRD, Rigaku D/Max-2400 X-ray diffractometer with Cu-Kα irradiation) at a scanning speed of 1.2°/min. The chemical states of the elements in the samples were determined using a PHI5702 multifunctional X-ray photoelectron spectroscope (XPS, USA). XPS analysis was conducted at 400 W and pass energy of 29.35 eV, using Al-Kα irradiation (1486.6 eV) as the excitation source, and the binding energy of contaminated carbon (C1s = 284.6

eV) was used as reference. The optical absorption was measured by a Spect-50 UV-vis spectrophotometer (Jena, Germany) in the wavelength range of 300-1100 nm. The photoelectrical conversion efficiency of the as-prepared samples was determined by a CELL-S500 (China) solar simulator at 100 $mW \cdot cm^{-2}$ (AM1.5G).

3. Results and discussion

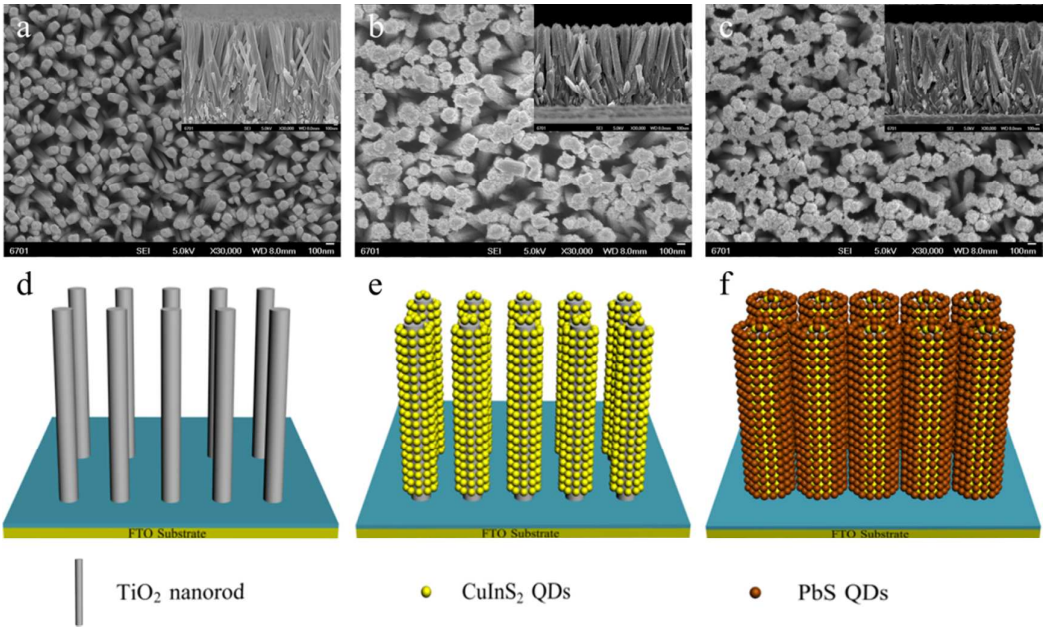

Fig. 1 Top-view FESEM images of (a) the plain TiO_2 nanorods, (b) $CuInS_2(6)/TiO_2$ and (c) $PbS(4)/CuInS_2(6)/TiO_2$. The insets show the cross-sectional view of the corresponding top-view FESEM images. 3D schematic diagrams of (d) the plain TiO_2 nanorods, (b) $CuInS_2(6)/TiO_2$ and (c) $PbS(4)/CuInS_2(6)/TiO_2$.

Fig. 1 presents the FESEM images of various as-prepared photoelectordes (a-c) and the corresponding 3D schematic diagrams of the photoelectrodes (d-f). Fig. 1a shows a typical top-view FESEM image of the plain TiO_2 nanorods. The TiO_2 nanorods with tetragonal crystal planes grow uniformly all over the FTO substrate

with an obvious porosity between them. The cross-sectional view in the inset of Fig. 1a demonstrates that the TiO_2 nanorods are vertically aligned and the length of TiO_2 nanorods is about 2 μm. The surface of TiO_2 nanorods becomes rough after the $CuInS_2$ QDs deposition for 6 circles (Fig. 1b) and the QDs are uniformly coated on TiO_2 nanorods. Fig. 1c presents the top-view and cross-sectional FESEM images of PbS(4)/$CuInS_2$(6)/TiO_2. It shows that the $CuInS_2$ QDs are aggregated on the top and side faces of TiO_2 nanorods and the PbS QDs are uniformly deposited on the $CuInS_2$/TiO_2 photoelectrode. As a result, the surface of photoelectrode becomes rougher than that in Fig. 1b.

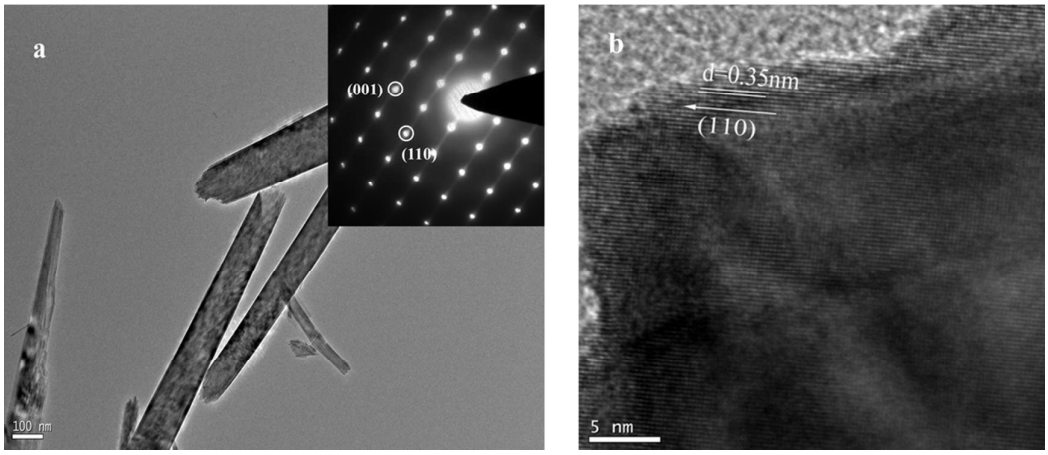

Fig. 2 TEM (a) and HRTEM (b) images of the plain TiO_2 nanorods. The inset in (a) is the selected-area electron diffraction pattern of TiO_2 nanorods.

Fig. 2 shows the TEM and HRTEM images of the plain TiO_2 nanorods. It can be found that the diameter of plain TiO_2 nanorod is around 130 nm (Fig. 2a). The SAED pattern (the inset in Fig. 2a) and the HRTEM image (Fig. 2b) confirm that the nanorods are single crystalline. The HRTEM image shows a (110) lattice spacing of

0.35 nm, and the nanorods grow along the (110) crystal plane with a preferred (001) orientation. The X-ray diffraction (XRD) spectrum displayed in Fig. 4 also confirms the single crystalline nature of TiO_2 nanorods, and the nanorods can be classified as tetragonal rutile phase (JCPDS file no. 21-1276) as all the characteristic peaks of TiO_2 nanorods agree well with rutile phase.

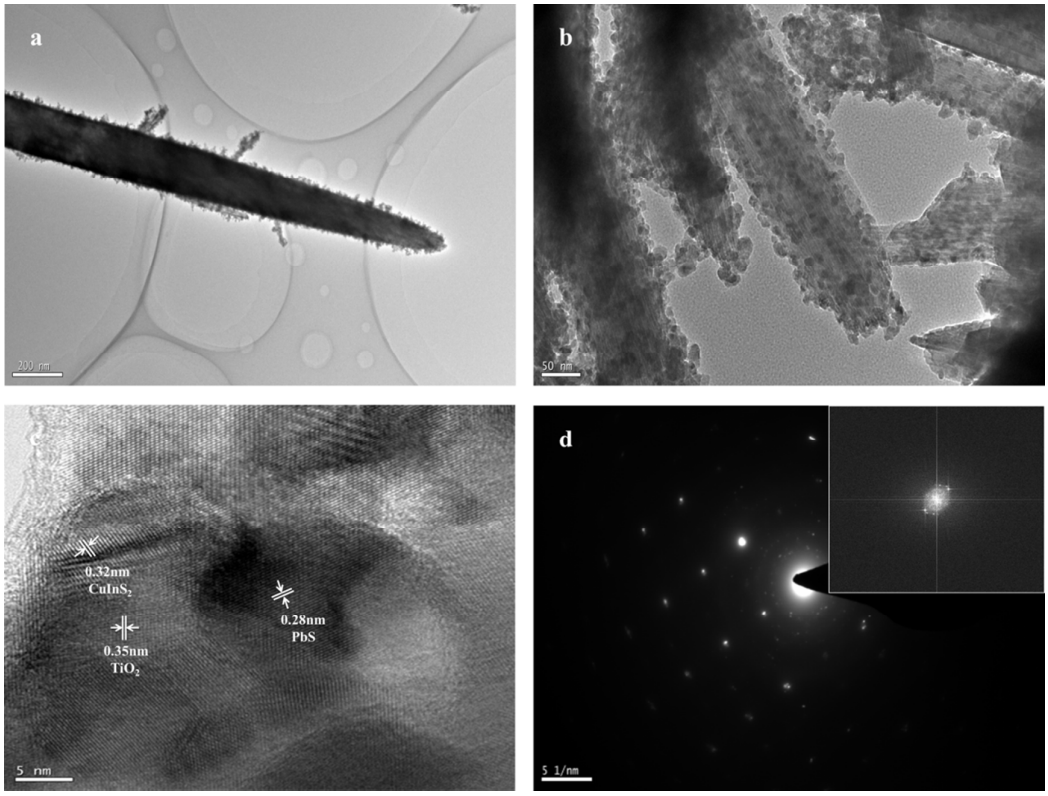

Fig. 3 TEM (a, b) and HRTEM (c) images of PbS(4)/$CuInS_2$(6)/TiO_2. The SAED pattern of PbS(4)/$CuInS_2$(6)/TiO_2 (d), the inset shows the electron diffraction pattern of a single QD.

Fig. 3a and b display the TEM images of PbS(4)/$CuInS_2$(6)/TiO_2. The nanorod structures of TiO_2 are not damaged during the $CuInS_2$ QDs and PbS QDs depositing process, and the QDs with a size ranging from 5 nm to 10 nm are uniformly covered

over the TiO_2 nanorods. Clearly distinguishable lattice fringes in the HRTEM image (Fig. 3c) verify the high crystallinity of the nanorods and QDs. The distance between lattice fringes is 0.32 nm and 0.28 nm, corresponding to the (112) plane of tetragonal $CuInS_2$ (JCPDS file no. 27-0159) and the (220) plane of cubic PbS (JCPDS file no. 159-0592), respectively. In addition, the lattice fringe distance of 0.35 nm is corresponding to the (110) plane of rutile phase of TiO_2. The SAED pattern of PbS(4)/$CuInS_2$(6)/TiO_2, is consist of many single crystal diffraction spots (Fig. 3d). The diffraction spots are in messy arrangement for the quantity and density of the QDs. The inset of the electron diffraction pattern of a single QD, indicates the QDs are of high crytallinity, which is consistent with the analysis in Fig. 3c. More detailed TEM images of PbS(*m*)/$CuInS_2$(*n*)/TiO_2 photoelectrodes are shown in the Supporting Information (Fig. S1, ESI).

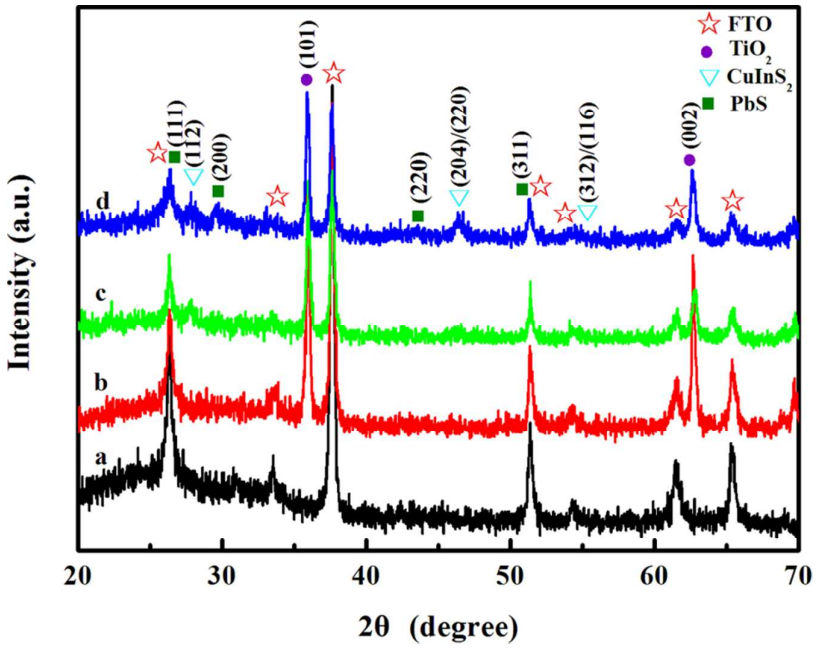

Fig. 4 Typical XRD patterns of the as-obtained photoelectrodes.

Fig. 4 shows the XRD patterns of the samples, where curve a, b, c and d represents the XRD pattern of FTO, TiO_2/FTO, $CuInS_2$(6)/TiO_2/FTO and PbS(4)/$CuInS_2$(6)/TiO_2/FTO respectively. Apart from the FTO substrate and TiO_2 film, the rest of the diffraction peaks well match the tetragonal $CuInS_2$ (JCPDS file no. 27-0159) and cubic PbS (JCPDS file no. 159-0592). The diffraction peaks located at the diffraction angle of 27.9^o, 46.2^o and 54.9^o are corresponding to the crystal planes of (112), (204)/(220) and (312)/(116) of the $CuInS_2$ QDs. At diffraction angle of 54.9^o, the diffraction peak widen obviously because the diffraction peaks of $CuInS_2$ and FTO coincide with each other. Meanwhile, the diffraction peaks at 25.9^o, 30.1^o and 43.1^o can be indexed to the crystal planes of (111), (200) and (220) of PbS QDs. At diffraction angle of 25.9^o, the diffraction peak also widen obviously as the diffraction peaks of PbS and FTO coincide with each other. The average diameter of $CuInS_2$ and PbS can be estimated by Scherrer's equation, $D = K\lambda/\beta\cos\theta$, where K is a shape factor equal to 0.89, λ is the wavelength of the X-ray equal to 1.5406 Å, β is the full-width at half maximum in radians calculated from the diffraction peak intensity and θ is the Bragg's angle. The calculation is done to get the average diameters of 9 nm for $CuInS_2$ and 6 nm for PbS, respectively, corresponding to the TEM images in Fig. 3. Moreover, the X-ray photoelectron spectroscopy (XPS) has also been performed to investigate the surface composition as well as valence state of PbS(4)/$CuInS_2$(6)/TiO_2. As shown in Fig. S2, all the peaks correspond to Ti, Cu, In, Pb, S, O and C elements (in which the C element was used to calibration) can be clearly detected and their valence states are consistent with the corresponding standardized binding energies.

Combined with the XPS analysis, it can be corroborated that the $CuInS_2$ QDs and PbS QDs are deposited on the surface of TiO_2 nanorods successfully and there is no obviously impurities exist in the as-obtained PbS(4)/$CuInS_2$(6)/TiO_2 samples.

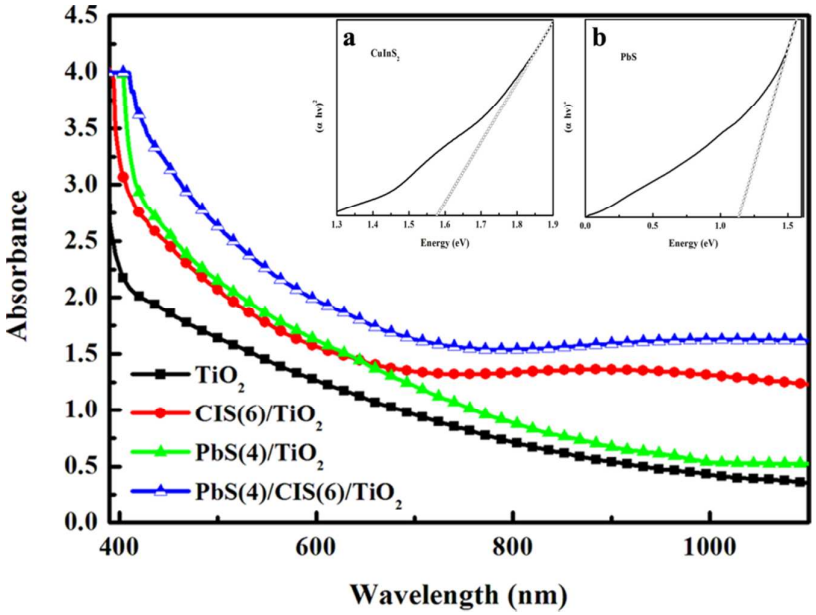

Fig. 5 UV-vis absorption spectra of the plain TiO_2 nanorods film and PbS(m)/$CuInS_2$(n)/TiO_2 films. The insets show the plots of $(\alpha hv)^2$ against photon energy (hv) for (a) $CuInS_2$ QDs and (b) PbS QDs, respectively.

Fig. 5 presents the variation of optical absorption for the plain TiO_2 nanorods and PbS(m)/$CuInS_2$(n)/TiO_2 films as a function of wavelength (CIS is short for $CuInS_2$). A generally increased optical absorption is observed for the PbS(m)/$CuInS_2$(n)/TiO_2 films compared with that of the plain TiO_2 nanorods, the absorption edge of which is only 400 nm. The deposition of $CuInS_2$ QDs and PbS QDs on TiO_2 nanorods enlarges the absorption edges to 650 nm and 900 nm respectively, which confirms that the $CuInS_2$ QDs and PbS QDs can effectively improve the light absorption property of the

TiO_2 nanorods. The insets of a and b show the plots of $(\alpha hv)^2$ against photon energy (hv) for $CuInS_2$ QDs and PbS QDs, and the band gap of $CuInS_2$ QDs and PbS QDs is determined to be 1.58 eV and 1.15 eV repectively according to the long wavelength extrapolation of the band gap. Compared with that of the bulk $CuInS_2$ and PbS, the band gaps of the two QDs all have changed, suggesting the presence of quantum size effect. Meanwhile, the band gap of $CuInS_2(6)/TiO_2$ and $PbS(4)/TiO_2$ electrodes is also calculated (Fig. S4, ESI), which indicats that the enhanced absorption in the longer wavelength region is due to the quantum confinement effect of the $CuInS_2$ and PbS QDs. Moreover, the $PbS(m)/CuInS_2(n)/TiO_2$ films enlarge the absorption edge to 750 nm, greater than that of 650 nm for $CuInS_2/TiO_2$ films, indicating that PbS is a promising co-sensitizer for the $CuInS_2/TiO_2$ QDSSCs and the co-sensitized films (i.e., the $PbS(m)/CuInS_2(n)/TiO_2$ films) have complementary and enhancement effects in light harvest, which is similar to the case of CdS and CdSe co-sensitized TiO_2 films.[35]

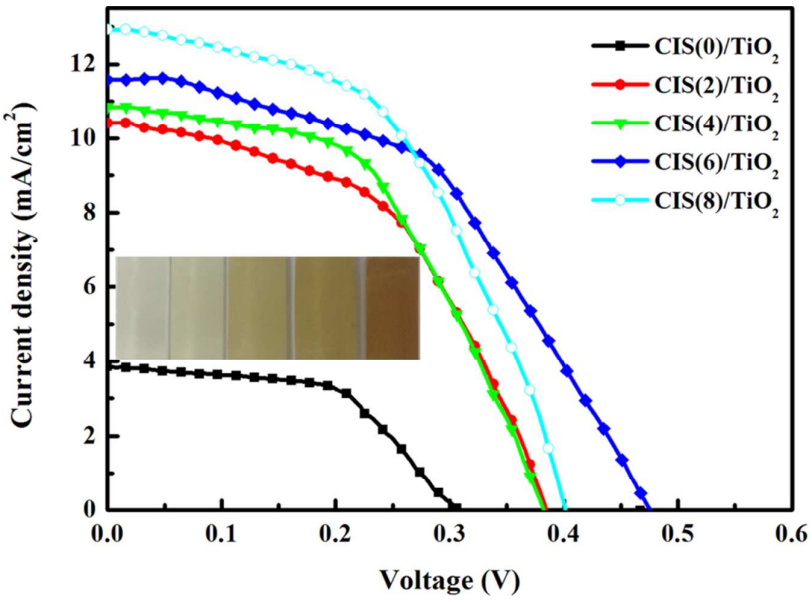

Fig. 6 J-V characteristics of QDSSCs employing $CuInS_2(n)/TiO_2$ photoelectrodes.

It is well known that the performance of QDSSCs depends on the SILAR cycles introduced to prepare the QDs-modified TiO_2 films. Therefore, the influence of SILAR cycles on the current density-voltage (J-V) characteristics is investigated. The J-V characteristics of QDSSCs employing $CuInS_2(n)/TiO_2$ photoelectrodes are shown in Fig. 6, and the corresponding parameters as open circuit potential (V_{OC}), short-circuit current density (J_{SC}), fill factor (FF) and energy conversion efficiency (η) are listed in Table 1. The inset in Fig. 6 shows the photos of $CuInS_2(n)/TiO_2$ photoelectrodes where the values of n are 0, 2, 4, 6, 8 from left to right, respectively. It can be found that the J_{SC} is enhanced with the increasing deposition cycles n of $CuInS_2$ QDs on TiO_2 nanorods, while the V_{OC} exhibits a tendency of increasing firstly and then decreasing. The QDSSC with $CuInS_2(6)/TiO_2$ photoelectrode reaches the maximum V_{OC} of 0.48 V and η of 2.61%. It could be concluded that the increasing quantity of $CuInS_2$ QDs on TiO_2 nanorods (the deepening color in the inset indicates the increasing quantity of $CuInS_2$ QDs on TiO_2 nanorods) raises the amount of semiconductor nanohybrid-heterojunctions consisting of $CuInS_2$ QDs and TiO_2, which increases the light absorption of QDSSCs and provides more channels for electron transportation, and enhances the collected photocurrent and energy conversion efficiency. However, for more deposition cycles ($n \geq 6$), the aggregation of excessive QDs weakens or even dissolves the quantum size effect (Fig. S1b, ESI), and it increases the series resistance of photovoltaic devices and the recombination loss of photogenerated carriers, leading to the decrease of energy conversion efficiency for QDSSCs.

Table 1 Photovoltaic parameters of QDSSCs employing various photoelectrodes.

Sample	V_{OC} (V)	J_{SC} (mA/cm^2)	FF	η (%)
CIS(0)/TiO_2	0.31	3.84	0.54	0.64
CIS(2)/TiO_2	0.38	10.68	0.47	1.91
CIS(4)/TiO_2	0.38	10.86	0.51	2.12
CIS(6)/TiO_2	0.48	11.60	0.47	2.61
CIS(8)/TiO_2	0.40	12.98	0.48	2.49
PbS(2)/CIS(6)/TiO_2	0.542	11.42	0.46	2.86
PbS(4)/CIS(6)/TiO_2	0.543	13.24	0.48	3.47
PbS(6)/CIS(6)/TiO_2	0.542	12.38	0.45	3.02
PbS(4)/CIS(0)/TiO_2	0.37	7.91	0.41	1.35
CIS(6)/PbS(4)/TiO_2	0.37	6.84	0.42	1.06
ZnS/PbS(4)/CIS(6)/TiO_2	0.57	14.52	0.50	4.11

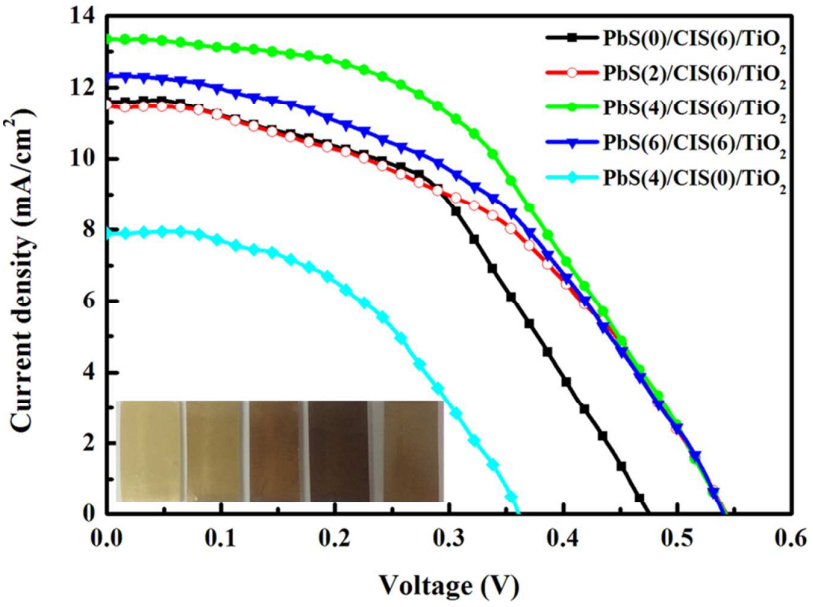

Fig. 7 J-V characteristics of QDSSCs employing PbS(*m*)/$CuInS_2$(6)/TiO_2 photoelectrodes.

Fig. 7 shows the J-V characteristics of PbS and $CuInS_2$ QDs co-sensitized QDSSCs by depositing PbS QDs on the $CuInS_2$(6)/TiO_2 electrodes and the corresponding parameters of PbS(*m*)/$CuInS_2$(6)/TiO_2 photoelectrode are listed in

Table 1. The inset in Fig. 7 shows the photos of PbS(*m*)/$CuInS_2$(6)/TiO_2 photoelectrodes where the values of *m* are 0, 2, 4, 6 from left to right respectively and the last sample is PbS(4)/$CuInS_2$(0)/TiO_2 electrode. The J_{SC} and V_{OC} of PbS(*m*)/$CuInS_2$(6)/TiO_2 photoelectrode are in a tendency of first increasing and then decreasing with the increasing deposition cycles *m* of PbS QDs. The QDSSC employing PbS(4)/$CuInS_2$(6)/TiO_2 electrode obtains the maximum η of 3.47%. This is due to the fact that the increasing amount of PbS QDs on $CuInS_2$(6)/TiO_2 photoelectrodes (the deepening of color in the inset indicates the increasing quantity of PbS QDs) increases the co-sensitization effect and improves η. While too much PbS QDs depositing ($m \geq 4$), similar to $CuInS_2$(*n*)/TiO_2, would lowered the quantum size effect and the high series resistance is predominant (Fig. S1d, ESI). Moreover, the energy conversion efficiency of PbS QDs-SSC is only 1.35%, which was due to the weak driving force of electron injection for PbS QDs. The conduction band edges of $CuInS_2$ and PbS for bulk phase are located above and below that of TiO_2[21,30], and it is difficult for the photoexcited electrons to inject into the next energy level, which leads to the lower value of J_{SC}, FF and η of single QDs sensitized TiO_2 photoelectrodes.

To understand the photogeneration process of the photovoltaic devices, the incident photon to current conversion efficiency (IPCE) spectra of QDSSCs assembled with various photoelectrodes measured from the I_{SC} monitored at different excitation wavelengths are presented in Fig. 8. It is clearly seen that the IPCE spectra of the devices are all consistent with the UV-vis absorption spectra in Fig. 5.

Compared with QDSSC assembled with PbS(4) /TiO_2 electrode, the QDSSC assembled with $CuInS_2$(6)/TiO_2 electrode obtain the IPCE value of 29%, higher than that of PbS-QDSSC, which suggests that the injection ability of photoexcited electrons for $CuInS_2$-QDSSC is stronger than PbS-QDSSC due to its higher conduction band edge. Furthermore, the IPCE value as high as 45% obtained by QDSSC assembled with PbS(4)/$CuInS_2$(6)/TiO_2 electrode in the wavelength range of 380-750 nm indicates that the deposition of $CuInS_2$ or PbS QDs systematically leads to higher external quantum efficiency, which is mainly due to the enlarged photoresponse range and enhanced photoelectron injection ability.

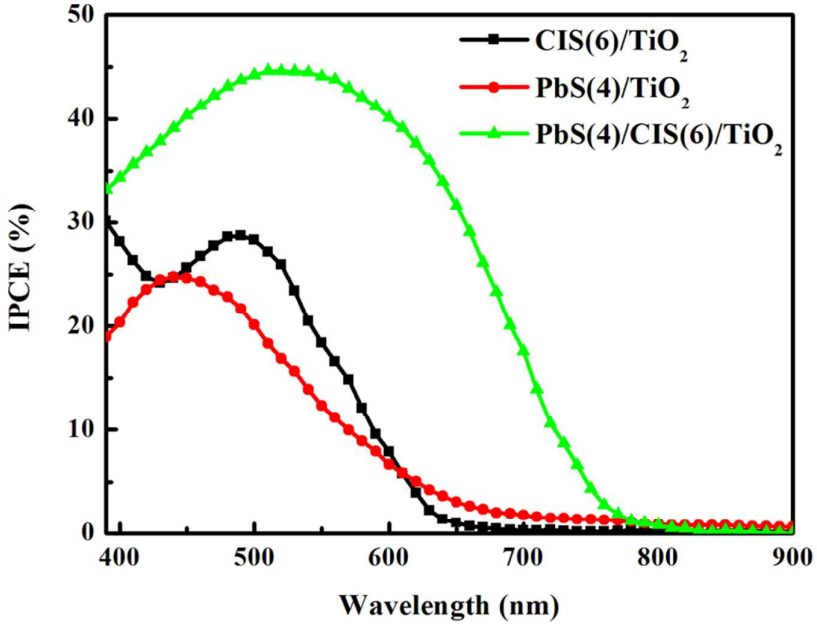

Fig. 8 Incident photon to current conversion efficiency (IPCE) spectra of QDSSCs assembled with PbS(*m*)/$CuInS_2$(*n*)/TiO_2 photoelectrode.

In order to further study the co-sensitization effect and the structure of QDSSCs, the PbS(4)/$CuInS_2$(6)/TiO_2 electrodes are prepared to investigate the effect of QDs co-sensitizers layers order on the photovoltaic performance of QDSSCs. The J-V

characteristics and corresponding parameters are presented in Fig. 9 and Table 1. The photovoltaic characteristic of QDSSC assembled with $CuInS_2(6)/PbS(4)/TiO_2$ electrode degrades dramatically compared with that of $PbS(4)/CuInS_2(6)/TiO_2$ electrode. The reason is laid in that the $CuInS_2$ QDs between TiO_2 nanorods and PbS QDs could enhanced the capacity of collecting excited electrons, and therefore, the co-sensitization effect is strengthened. However, the electronic transitions are restrained and the co-sensitization effect cannot be realized when the PbS QDs are deposited between TiO_2 nanorods and $CuInS_2$ QDs. It can also be determined that the $PbS/CuInS_2/TiO_2$ electrode is a cascade structure as the STEM shows in Fig. S3 which is similar to the $CdSe/CdS/TiO_2$ electrode.[35]

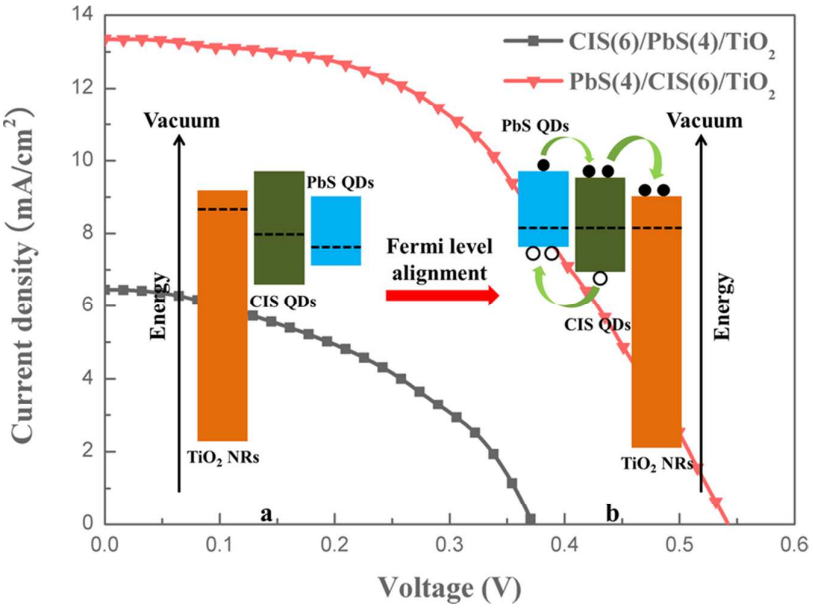

Fig. 9 Schematic diagram of the energy level arrangement of TiO_2, $CuInS_2$ and PbS in bulk phase (a), and a possible structure and electron-hole transfer pathways for $PbS/CuInS_2/TiO_2$ photoelectrodes after Fermi level alignment (b). J-V characteristics of QDSSCs employing $CuInS_2(6)/PbS(4)/TiO_2$ (square) and $PbS(4)/CuInS_2(6)/TiO_2$

photoelectrodes (triangle).

Compared with QDSSCs fabricated with $CuInS_2/TiO_2$, the photoelectrochemical characteristic of the QDSSC fabricated with $PbS/CuInS_2/TiO_2$ electrode has some increment, which is attributed to the Fermi level alignment. Fig. 9a displays the energy level arrangement of TiO_2, $CuInS_2$ and PbS in bulk phase which can be found elsewhere.[21, 31, 37] When the PbS QDs and $CuInS_2$ QDs contact with each other and form the cascade structure on the TiO_2 nanorods, the electrons will transfer from the high energy level to the low energy to achieve an energy balance because of the Fermi level difference, which is denoted as Fermi level alignment. The redistribution of electrons rearranges the energy level of TiO_2, $CuInS_2$ and PbS (Fig. 9b). The deposition of PbS QDs on the $CuInS_2/TiO_2$ electrode enlarges the absorption range and increases the photocurrrent of co-sensitized QDSCs, which enhanced the photovoltaic characteristic of QDSSCs eventually. On the other hand, the presence of $CuInS_2$ QDs between PbS QDs and TiO_2 nanorods enhances the conduction band edge of PbS QDs relatively because of the redistribution of electrons, providing a more powerful driving force for the injection of photoexcited electrons into the next energy level. Hence the electrons density transferring to the FTO substrates is increased and the recombination of photogenerated carriers is restained as well. As a result, the collected current of $PbS/CuInS_2/TiO_2$ electrodes is enhanced. Meanwhile, the cascade structure of $PbS/CuInS_2/TiO_2$ electrodes reduces the band bending at the TiO_2 interface, which is benefit to the injection of photoexcited electron to TiO_2. Therefore, the performances of photovoltaic devices are enhanced. Moreover, the EIS

Nynquist plots of various photoelectrodes are measured and shown in Fig. S5. The deposition of $CuInS_2$ and PbS QDs could greatly and effectively improve the separation of photo-generated electron–hole pairs. Simultaneously, it could accelerate the interfacial charge transfer and electron injection process. In addition, the Mott-Schottky plot of PbS/$CuInS_2$/TiO_2 photoelectrodes (Fig. S6) shows that the charge carrier density of photoelectrode increases with the deposition of $CuInS_2$ and PbS QDs, which could lead to the upwards shift of the Fermi level, and the conduction band of $CuInS_2$ and PbS QDs is enhanced relatively. Simultaneously, the enlarged band gap of QDs could enhance the conduction band of semiconductor QDs, which lead to the expected higher conduction band of PbS QDs coupled with the upwards shift of the Fermi level as shown in Fig. 9b. Overall, the cascade structure takes the advantages both of PbS QDs and $CuInS_2$ QDs, achieving the synergistic effect, and increases the energy conversion efficiency eventually, which is the practical significance of co-sensitization effect.

To further improve the performance of the as-prepared photovoltaic devices, a ZnS passivation layer prepared according to the literature is used to retard the back transfer of electrons and protect the QDs from photocorrosion.[38,39] The introduction of ZnS passivation layer could increase the V_{OC}, J_{SC} and FF, and the energy conversion efficiency η increases from 3.47% to 4.11% (Fig. 10, and Table 1). As previous studies reveal, there is no meaningful change in the UV-vis spectrum, but the dark current decreases after the deposition of ZnS, which indicates that the ZnS passivation layer as an effective intermediate layer between photoelectrode and electrolyte could

suppress the electrons leakage from TiO_2 to the electrolyte and avoid the direct electrons recombination in the interface of TiO_2 and electrolyte, increasing charge collecting efficiency and energy conversion efficiency η.

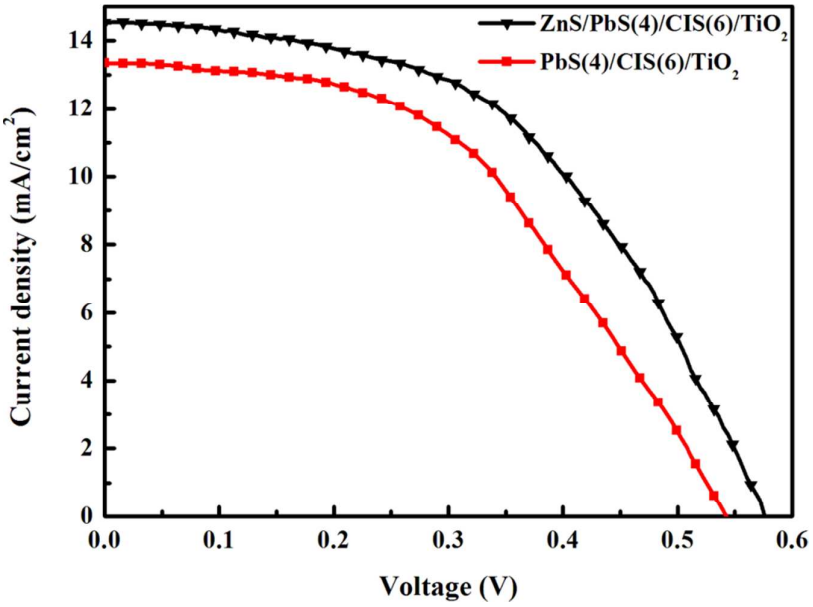

Fig. 10 Effects of ZnS passivation layer on the J-V characteristics of QDSSCs assembled with PbS(4)/$CuInS_2$(6)/TiO_2 photoelectrode.

4. Conclusions

In this work, a cascade structure of PbS/$CuInS_2$/TiO_2 electrodes with the co-sensitization effect is prepared with the SILAR method. The SILAR cycles of *n* and *m* for $CuInS_2$ QDs and PbS QDs are discussed carefully and it is found that the performance of QDSSCs depends on the value of *n* and *m* dominantly. Moreover, the contact of PbS QDs and $CuInS_2$ QDs on the surface of TiO_2 nanorods can alter the energy level arrangement of TiO_2, $CuInS_2$ and PbS into an energy level order of PbS > $CuInS_2$ > TiO_2, which increases the driving force for electrons injection and inhibits the recombination of photogenerated carriers. Under one sun illumination, the cascade

structure obtains the maximum η value of 4.11%.

Appendix A. Electronic Supplementary Information

Acknowledgements

The authors gratefully acknowledge the National Natural Science Foundation of China (Grant No. 51175490, 51170116) for providing the financial support.

REFERENCES

(1) P. V. Kamat, *J. Phys. Chem. C*, 2008, **112**, 18737-18753.

(2) K. P. Wang, H. Teng, *Phys. Chem. Chem. Phys.*, 2009, **11**, 9489-9496.

(3) S. Rühle, M. Shalom, A. Zaban, *ChemPhysChem*, 2010, **11**, 2290-2304.

(4) A. Kongkanand, K. Tvrdy, K. Takechi, M. Kuno, P. V. Kamat, *J. Am. Chem. Soc.*, 2008, **130**, 4007-4015.

(5) S. Mathew, A. Yella, P. Gao, R. Humphry-Baker, B. F. E. Curchod, N. Ashari-Astani, I. Tavernelli, U. Rothlisberger, M. K. Nazeeruddin, M. Grätzel, *Nature Chem.*, 2014, **6**, 242-247.

(6) P. K. Santra, P. V. Kamat, *J. Am. Chem. Soc.*, 2012, **134**, 2508-2511.

(7) W. W. Yu, L. Qu, W. Guo, X. Peng, *Chem. Mater.*, 2003, **15**, 2854-2860.

(8) V. I. Klimov, *J. Phys. Chem. B*, 2006, **110**, 16827-16845.

(9) M. N. Tahir, P. Theato, P. Oberle, A. Janshoff, M. Stepputat, W. Tremel, *Langmuir*, 2006, **22**, 5209-5212.

(10) H. Wang, Y. Bai, H. Zhang, Z. Zhang, J. Li, L. Guo, *J. Phys. Chem. C*, 2010, **114**, 16451-16455.

(11) Y. Xie, G. Ali, S. H. Yoo, S. O. Cho, *ACS Appl. Mater. Interfaces*, 2010, **2**, 2910-2914.

(12) J. H. Bang, P. V. Kamat, *ACS Nano*, 2009, **3**, 1467-1476.

(13) R. Wang, L. Wan, H. Niu, Q. Ma, S. Miao, J. Xu, *J. Sol-Gel Sci. Technol.*, 2013, **67**, 458-463.

(14) H. J. Lee, M. Wang, P. Chen, S. M. Zakeeruddin, M. Grätzel, M. K. Nazeeruddin, *Nano Lett.*, 2009, **9**, 4221-4227.

(15) Q. Dai, J. Chen, L. Lu, J. Tang, W. Wang, *Nano Lett.*, 2012, **12**, 4187-4193.

(16) A. Zaban, O. I. Micic, B. A. Gregg, A. J. Nozik, *Langmuir*, 1998, **14**, 3153-3156.

(17) P. Yu, K. Zhu, A. G. Norman, S. Ferrere, A. J. Frank, A. J. Nozik, *J. Phys. Chem. B*, 2006, **110**, 25451-25454.

(18) V. González-Pedro, C. Sima, G. Marzari, Q. Shen, T. Dittrich, I. Mora-Seró, *Phys. Chem. Chem. Phys.*, 2013, **15**, 13835-13843.

(19) L. M. Peter, K. G. U. Wijayantha, D. J. Riley, J. P. Waggett, *J. Phys. Chem. B*, 2003, **107**, 8378-8381.

(20) M. Sun, D. Zhu, W. Ji, X. Wang, W. Xiang, J. Zhao, *ACS Appl. Mater. Interfaces*, 2013, **5**, 12681-12688.

(21) J. Y. Chang, J. M. Lin, L. F. Su, C. F. Chang, *ACS Appl. Mater. Interfaces*, 2013, **5**, 8740-8752.

(22) C. Chen, G. Ali, S. H. Yoo, J. M. Kum, S. O. Cho, *J. Mater. Chem.*, 2011, **21**, 16430-16435.

(23) W. Yue, S. Han, R. Peng, F. Wu, S. Tao, M. Wang, *J. Mater. Chem.*, 2010, **20**, 7570-7578.

(24) H. Zhong, Y. Zhou, M. Ye, C. He, C. Yang, Y. Li, *Chem. Mater.*, 2008, **20**, 6434-6443.

(25) P. K. Santra, P. V. Nair, K. G. Thomas, P. V. Kamat, *J. Phys. Chem. Lett.*, 2013, **4**, 722-729.

(26) T. L. Li, H. Teng, *J. Mater. Chem.*, 2010, **20**, 3656-3664.

(27) T. L. Li, Y. L. Lee, H. Teng, *Energy Environ. Sci.*, 2012, **5**, 5315-5324.

(28) T. L. Li, Y. L. Lee, H. Teng, *J. Mater. Chem.*, 2011, **21**, 5089-5098.

(29) C. Sun, Z. Cevher, J. Zhang, B. Gao, K. Shumc, Y. Ren, *J. Mater. Chem. A*, 2014, **2**, 10629-10633.

(30) B. R. Hyun, Y. W. Zhong, A. C. Bartnik, J. R. Matthews, T. M. Leslie, N. F. Borrelli, *ACS Nano*, 2008, **2**, 2206-2212.

(31) H. Lee, H. C. Leventis, S. J. Moon, P. Chen, S. Ito, S. A. Haque, T. Torres, F. Nuesch, T. Geiger, S. M. Zakeeruddin, M. Grätzel, M. K. Nazeeruddin, *Adv. Funct. Mater.*, 2009, **19**, 2375-2742.

(32) F. Shen, W. Que, Y. Liao, X. Yin, *Ind. Eng. Chem. Res.*, 2011, **50**, 9131-9137.

(33) B. Liu, E. S. Aydil, *J. Am. Chem. Soc.*, 2009, **131**, 3985-3990.

(34) Y. L. Lee, C. H. Chang, *J. Power Sources*, 2008, **185**, 584-588.

(35) Y. L. Lee, Y. S. Lo, *Adv. Funct. Mater.*, 2009, **19**, 604-609.

(36) N. Osada, T. Oshima, S. Kuwahara, T. Toyoda, Q. Shen, K. Katayama, *Phys. Chem. Chem. Phys.*, 2014, **16**, 5774-5778.

(37) I. Ka, B. Gonfa, V. Le Borgne, D. Ma, M. A. El Khakani, *Adv. Funct. Mater.*, 2014, **24**, 4042-4050.

(38) N. Guijarro, J. M. Campiña, Q. Shen, T. Toyoda, T. Lana-Villarreal, R. Gómez, *Phys. Chem. Chem. Phys.*, 2011, **13**, 12024-12032.

(39) Y. Chen, Q. Tao, W. Fu, S. Su, P. Wang, M. Li, *Electrochim. Acta*, 2014, **118**, 176-181.

Table of Contents entry

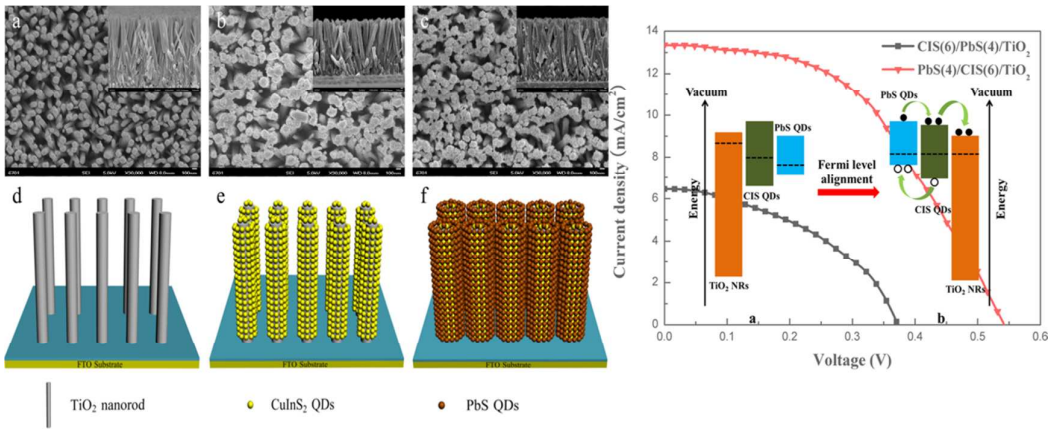

A cascade structured PbS/$CuInS_2$/TiO_2 photoelectrode with co-sensitization effect obtains the energy conversion efficiency of 4.11% under one sun illumination.